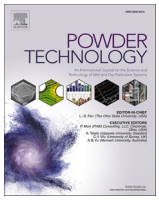
Powder Technology 466 (2025) 121417



Contents lists available at ScienceDirect

Powder Technology

journal homepage: www.journals.elsevier.com/powder-technology



Discrete element modelling of the mechanical evolution of a lithium-ion battery electrode layer following charge cycling

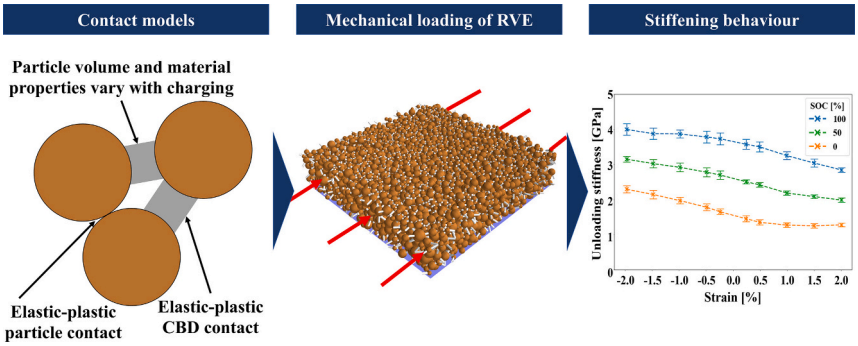
Axel Lundkvist [a], Per-Lennart Larsson [a], Erik Olsson [b,*]

[a] Department of Engineering Mechanics, Division of Material and Structural Mechanics, Royal Institute of Technology – KTH, Teknikringen 8, 100 44 Stockholm, Sweden
[b] Department of Engineering Sciences and Mathematics, Division of Solid Mechanics, Luleå University of Technology, Luleå, Sweden

HIGHLIGHTS

- DEM model for assessing Li-battery electrode's mechanical properties under charging
- The model explores the impact of NMC volumetric change related to charge cycling.
- Volumetric expansion of NMC leads to a stiffer electrode layer.

GRAPHICAL ABSTRACT



ARTICLE INFO

Keywords:
Discrete element method
Lithium-ion batteries
Mechanical characterisation
Mechanical degradation
Swelling
Charge cycling
Simulations

ABSTRACT

Mitigating the loss of charge capacity is one of the main challenges in developing lithium-ion batteries. Mechanical degradation is one of the causes of charge capacity loss, and insight into these processes is necessary for battery development. This study uses a discrete element method (DEM) framework to model the mechanical properties of a positive electrode active layer. In particular, how the active layer properties are affected by the volumetric change and material degradation of the active material linked to charge cycling. The results show a stiffening of the active layer following charge cycling, stemming from the volumetric expansion of the active particles. These results agree with trends seen in experimental measurements.

1. Introduction

Effective energy storage systems are crucial in the transition to renewable energy systems. Lithium-ion batteries (LIB) have emerged as one of the primary battery technologies during the 21st century. Due to its high energy density and rapid rechargeability, it has proven to be particularly effective in portable devices such as electric vehicles. The development of LIBs is, however, still ongoing to meet the requirements of the electric automotive industry. One of those requirements is a long lifetime of the batteries, as replacing them is both expensive and cumbersome. Currently, LIBs suffer from loss of charge capacity over charge cycling, which limits their life. Several mechanisms contribute to

* Corresponding author.
E-mail address: erik.1.olsson@ltu.se (E. Olsson).

https://doi.org/10.1016/j.powtec.2025.121417
Received 23 December 2024; Received in revised form 9 July 2025; Accepted 16 July 2025
Available online 18 July 2025
0032-5910/© 2025 The Authors. Published by Elsevier B.V. This is an open access article under the CC BY license (http://creativecommons.org/licenses/by/4.0/).

this charge degradation, and historically, the chemical degradation of the cells has mainly been studied [1]. However, the literature has shown that mechanical degradation processes also contribute to the loss of charge capacity [2]. Therefore, the mechanics of LIBs must be understood to mitigate the mechanical charge degradation.

Mechanical degradation of the LIB can be observed on all length scales within the battery. For the positive electrode, the mechanical degradation mechanism ranges from delamination of the active electrode layer from the current collector to cracking of the active material [1]. These damage mechanisms have been studied through experiments and simulation models [3–7]. On the length scale of the active material, the constituents of the electrode have been studied using various micro−/nanomechanical testing methods, such as nanoindentation and micro-cantilever bending tests, as well as non-destructive methods such as X-ray computed tomography (XCT) and X-ray diffraction (XRD). However, most of these experiments have been performed on uncycled specimens and do not capture the mechanical degradation of the active layer constituents over cycling. There have, however, been some studies where the mechanical properties over charge cycling have been investigated. Studies of the evolution of the active material polycrystalline NMC over charge cycling via XCT and XRD have resulted in counterintuitive observations. Polycrystalline NMC consists of spherical agglomerates (secondary particles) of single NMC crystals (primary particles). While the XRD showed a decrease in the crystal lattice unit volume of the primary particles during delithiation (i.e. during charging) between 1 and 6 % for different compositions of NMC at different delithiation states [8], XCT showed an increase in the volume of the secondary particles. Parks et al. [9] could show a volume increase between 13.3 and 28.3 % of NMC811 particles over the first delithiation, with an average volumetric increase of 20 %. This volume increase in the secondary particles is attributed by the authors [9] to intergranular and transgranular cracks and voids forming through and between the primary particles. The anisotropic expansion/contraction of the crystal plane directions of the primary particles enables the fracture mechanism. The following lithiation (discharge) showed cracks closing and the volume of the secondary particle decreasing, but not to its initial volume. Over charge cycling, more damage in the secondary particle particles remained, indicating a permanent expansion of the particles following the number of charge cycles [9–12]. Similar damage behaviour has also been seen through simulations [3,13]. Using the finite element method, Shishvan et al. [13] could show that the volume change of the primary particles resulted in internal stresses within the secondary particle, leading to fracture in the grain boundaries. Nanoindentation of the active material has also been performed over one charge cycle and after charge cycling. Xu et al. [14] showed that for NMC811, the Youngs modulus and the hardness of the NMC811 material decreased by roughly 20 % between 0 and 100 % state of charge (SOC) of the battery at the first delithiation. They could also show a gradual degradation in both the Youngs modulus and the hardness over charge cycling, with the most severe drop occurring after the first charge cycle. The drop in mechanical properties is argued by the authors [14] to stem from damage, such as cracks, forming in the material.

On the full electrode length scale, the evolution of the electrode properties has been studied through dilatometry measurements, indentations and bending tests. Dilatometry measurements of the positive electrode thickness over cycling showed a reversible and irreversible change in the cathode thickness. Whether the layer increased or decreased in height depends on the type of active material and to which voltages the electrode was cycled between. However, all tested cathodes showed some height increase during charging (i.e. delithiation of the active material) [15,16]. The evolution of the in-plane stiffness in compression of the positive electrode active layer over charge cycling was studied by Gupta et al. [17] using a bending test method. They could show that the in-plane stiffness increased both over charge cycling and at increased compression levels. This was motivated by an increased number of particles coming into contact following their expansion.

It is, however, essential to link the behaviours on different length scales to fully grasp the evolution of the mechanical behaviour of the electrode. For this purpose, numerical modelling is an invaluable tool. The discrete element method (DEM) has proved helpful for simulating mechanical properties and processes on the electrode scale. DEM enables the linking of the behaviour of the active material and the conductive binder domain (CBD), consisting of a blend between Polyvinylidene fluoride (PVDF) and carbon black (CB), to the behaviour of the full electrode layer while accurately capturing the electrodes' granular microstructure. This provides further insight into the interplay between mechanisms on different length scales, which can be challenging to determine through experimental methods. The main application of DEM on electrode layers has been for the manufacturing process, mainly the calendering process. However, properties such as electrical/ionic conductivity and heat transfer have also been modelled [18–21]. Sangrós Giménez et al. [22] also studied some interesting aspects of mechanical modelling over charge cycling, but again, the electrical and ionic behaviour was the main focus of the study. In our previous work [23,24], we have studied several aspects of the mechanical behaviour of a positive electrode layer by developing a DEM modelling framework. By evaluating the calendering process and the in-plane stiffness of the active layer, the interaction between properties of the binder domain and the active material has been established, as well as the impact of contact modelling for the layer constituents and the impact of material properties such as plasticity and viscoelasticity. The primary outcome of these two studies was that the mechanical behaviour of the active electrode layer is governed by both the active material and the binder domain. The layer is pressure-dependent, showing an increased stiffness at increased compression levels due to the increased contact between the active material. The layer also shows relaxation behaviours due to the viscoelastic binder domain.

In this study, we will further develop this DEM framework to extend the investigation of the mechanical properties of the electrode active layer. The investigation will focus on the varying mechanical properties of the active material during the change/discharge process of the LIB, as well as over several charge cycles. This is done by modelling the volumetric change and the variation of material properties that arise due to varying lithiation levels in the active material over charge cycling. The electrochemical process is not simulated explicitly; instead, the changed mechanical properties, stemming from the electrochemical reactions, are used as inputs for the mechanical model. The impact of these phenomena will be evaluated through two studies. One over the first delithiation of the layer, and the other where the layer is studied over several charge cycles. To the authors' knowledge, no studies in the literature have investigated how charge cycling changes the mechanical properties of the electrode layer and, in particular, how the behaviour of the active material is linked to the behaviour of the full electrode layer over cycling. This link between the usage of the LIB and the evolution of its mechanical properties is indeed essential to mitigate the mechanical degradation of the electrode.

2. Contact models

The behaviour of the electrode layer is governed by the interaction of its constituents, i.e. the active material and the CBD. The interaction of these constituents is determined in the DEM framework by prescribed contact models between the discrete elements. Two contact models are used in our framework. The first considered active particles in contact, and the second one considered active particles separated by the CBD. Principle sketches of the contacts and their respective force-overlap relations are presented in Fig. 1. Both types of contacts are also compatible with rigid walls. As for the particle contact, the rigid wall is treated as a rigid particle with an infinite radius.

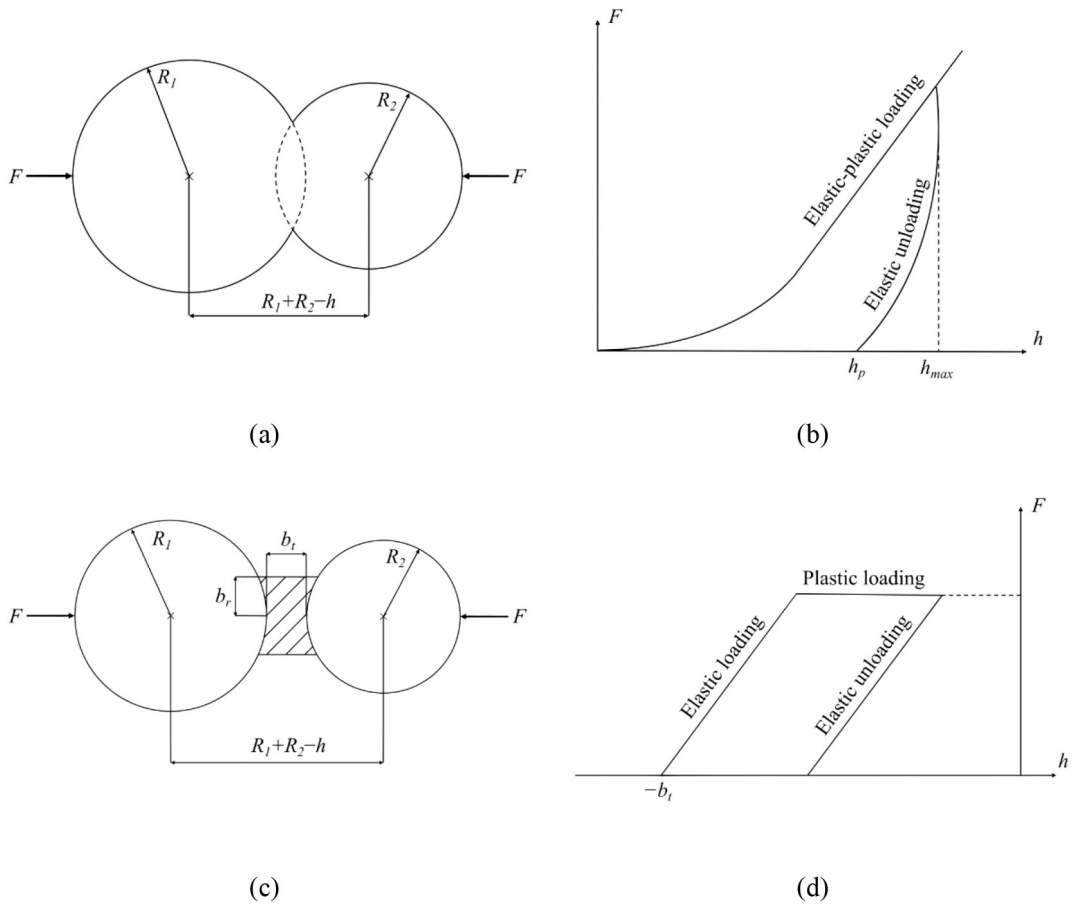


Fig. 1. Sketches of the contact and corresponding force-overlap relation for the particle contact, (a) and (b), and the CBD contact, (c) and (d). Figures adapted from [23].

2.1. Active particles

The contact model used for the active particles is based on elastic-plastic contact mechanics to describe their force-overlap relation. It is, at large, the same contact formulation used in our previous study [24] and will briefly be summarised hereunder.

The Brinell indentation process of an elastic-plastic material, relevant for the present purpose as discussed below, was studied by Johnson [25], where he proposed that the indentation process can be divided into three regions governed by the properties of the indented material. In Region I, the contact is dominated by elastic deformation of the material. In Region II, the indentation is governed by both elastic and plastic deformation of the material. In the final region, Region III, the indentation is governed by large plastic deformations and elasticity can be neglected. The indentation can be described by two dimensionless parameters: the normalised hardness $\overline{H}$ and a contact area parameter c^2. The normalised hardness is defined as

$$\overline{H} = \frac{F}{\pi a^2 \sigma_{rep}} \quad , \tag{1}$$

where F is the indentation force, a is the contact radius and σ_{rep} is the yield strength at a representative value of the plastic strain. For an elastic-perfectly plastic material σ_{rep} is the initial yield strength σ_Y. The contact area parameter is defined as

$$c^2 = \frac{a^2}{2hR} \quad , \tag{2}$$

where h is the indentation depth and R is the radius of the indenter. This study assumes a perfectly plastic material, which entails a yield strength independent of the magnitude of the plastic strain. Both the normalised hardness and the contact area parameter can be related to a dimensionless loading parameter Λ, defined as

$$\Lambda = \frac{E}{(1-\nu^2)\sigma_{rep}} \frac{a}{R} \quad , \tag{3}$$

where E and ν are the materials' Young's modulus and Poisson's ratio, respectively.

In the initial elastic region, the contact can be described by Hertz contact theory [26]. In the final plastic contact region, the contact can be described by self-similarity solutions, and $\overline{H}$ and c^2 take on constant values independent of the loading Λ [27–29]. For the second contact region, where both elastic and plastic deformation must be considered, no closed-form solution for the normalised hardness or the contact area has been presented in the literature. Through extensive finite element analysis of Brinell indentations, Olsson and Larsson [30,31] could show that both the normalised hardness and the contact area parameter could be fitted to master curves, dependent on the loading parameter Λ. The hardness for all three contact regions is then given by

$$\overline{H} = \begin{cases} \frac{4}{3\pi}\Lambda & \Lambda < 3 \\ \overline{H}_{max} - 0.0965(\ln\Lambda - \ln 160)^2 & 3 \le \Lambda \le 160 \\ \overline{H}_{max} & \Lambda > 160 \end{cases} \tag{4}$$

where $\overline{H}_{max} = 3$ and the contact area parameter is given by

$$c^2 = \begin{cases} 0.5 & \Lambda < 4 \\ 1.1355x + 0.519x^2 + 0.5 & 4 \leq \Lambda \leq 1527 \\ 1.43 & \Lambda > 1527 \end{cases} \quad (5)$$

where $x = \frac{\ln\Lambda - \ln 4}{\ln 1527 - \ln 4}$.

These contact relations for the Brinell indentation in the spirit of Hertz [28] can be used to describe the contact between two spherical particles under the assumption that the contact surface is also spherical. This contact can also be represented by each particle being indented by a rigid surface with a curvature of plus/minus the curvature of the contact respectively. These two indentations can be equated to a rigid sphere indenting an elastic-plastic half-space. The solution to the contact problem between the two spheres is found when the two indentations of the half-spaces give the same contact force/contact area. These relations can then be solved for a range of contact forces, providing relations for contact force/area to the indentation depth. Olsson and Larsson [31] could also show that the contact relations between spherical particles of dissimilar sizes could be generalised if the contact force is normalised with the yield strength σ_Y and the effective radius of the contact pair R^*, defined by

$$R^* = \left(\frac{1}{R_1} + \frac{1}{R_2}\right)^{-1} , \quad (6)$$

where R_1/R_2 is the radius of the two particles in the contact pair. This enables the use of one master curve of the normalised force-overlap relation in the contact model for all the particles. The master curve is accurately described by a four-parameter power function on the form

$$\overline{F}\left(\frac{h}{R^*}\right) = \overline{F}_1\left(\frac{h}{R^*}\right)^{\alpha_1} + \overline{F}_2\left(\frac{h}{R^*}\right)^{\alpha_2} , \quad (7)$$

where h is the contact overlap and

$$\overline{F}_i = \frac{F_i}{\sigma_Y R^{*2-\alpha_i}} . \quad (8)$$

This normalisation also provides the same master curve for elastic-perfectly plastic materials with different properties, as long as the ratio between the modulus and the yield strength is similar. Using this master curve proves the evaluation of the contact forces in the DEM code effective, requiring only the normalised overlap of the particles in the contact pair as input at each iteration. For the complete derivation and motivation of these contact relations, the reader is referred to the study by Olsson and Larsson [31]. Unloading of particle contacts is performed in an elastic manner, following Hertz contact, as described in our previous study [23]. Friction between the particles is not considered with the motivation that Olsson and Larsson [32] could show that the impact of friction is negligible on compaction stiffness, especially when considering the CBD's shear stiffness.

In order to capture the degradation of the material properties, both over one charge cycle and over charge cycling, as shown by Xu et al. [14], the modulus and yield strength, will be scaled with a degradation factor κ, dependent on either the SOC over the cycle or the number of cycles. As the ratio between the modulus and the yield strength is reasonably constant at degradation, this is a viable approach to model the material degradation in our DEM framework. The charge cycling also entails a change in the volume of the active particles, as indicated in the literature. This is represented by altering the radius of the particles, dependent on either the SOC over the cycle or the number of cycles. This change in radius leads to a change in the effective radius of the contact as well as a change in the contact overlap (if the positions of the particles are constant).

2.2. Conductive binder domain

The CBD is modelled as a cylinder between the two particles in the contact pair. The CBD contact is load-bearing in tension, compression, and shearing, giving structural rigidity to the active layer. The dimensions of the cylinder, i.e. the radius and height, depend on the radius of one of the particles in the contact pair. The particle on which the dimensions should be based on is determined randomly at the initiation of the contact. If the contact is initiated between a particle and a rigid surface, the radius from the particle is used. The ratio of the CBD radius to particle radius is set to $\frac{b_r}{R} = 1.75$, and the CBD height to particle radius is set to $\frac{b_t}{R} = 0.5$. It should be noted that the dimensions of the CBD does not change when the radius of the particles is altered, as the dimensions of the CBD is determined only at the initiation of the contact. The material for the CBD is modelled as elastic-perfectly plastic, and the force-overlap relation in the normal direction is given by

$$F_n = \frac{(1-\nu)EA}{(1+\nu)(1-2\nu)} \frac{h + b_t}{b_t} , \quad (9)$$

while it in the tangential direction is given by

$$F_t = \frac{EA}{2(1+\nu)} \frac{u}{b_t} . \quad (10)$$

As seen in eq. (9), the overlap is shifted with the CDB thickness, this as the overlap is defined with respect to the particles' surfaces being in contact. Here A is the cross-sectional area of the CBD cylinder, and u is the tangential displacement. Yielding is determined by evaluating the magnitude of the normal stress against the yield strength, and further loading after yielding results in a constant force due to perfect plasticity. Unloading after yielding occurs in an elastic manner, according to eq. (9). The CBD contact also incorporates a damper with the sole purpose of stabilising the simulations. The damper operates as a viscoelastic standard linear solid element in Maxwell representation. The ratio between the instantaneous and the relaxed stiffness was 0.75, and the Maxwell element's relaxation time was magnitudes shorter than the loading times used in the simulations and will thus not affect the results.

3. Simulation setup

The above-described contact models have been used in a DEM framework to investigate the relation between the contact behaviour of the active particles and the CBD and the mechanical behaviour of the full electrode layer. The developed framework will briefly be summarised here, but it has been thoroughly described in our previous studies [23,24]. The framework is built on an in-house DEM code, using standard formulations, and its main purpose is to model the mechanical behaviour of a positive electrode's active layer. A flowchart of the iterative DEM calculation can be seen in Fig. 2. The electrode is formed by a network of active particles in contact as well as active particles separated by the CBD. Each active particle is represented by a discrete element. The interaction between the active particles and the active particles separated by the CBD is governed by the contact models, as described in the previous chapter. A representative volume element (RVE), with in-plane periodic boundary conditions and 5000 active particles, is used to represent a quasi-infinite electrode layer. The size of the RVE sides is determined at the initialization of the simulation, following a prediction of the final density of the electrode layer. A rigid surface is placed at the bottom of the RVE, representing the current collector of the electrode. The material properties used for the active material (before degradation) and the CBD can be seen in Table 1.

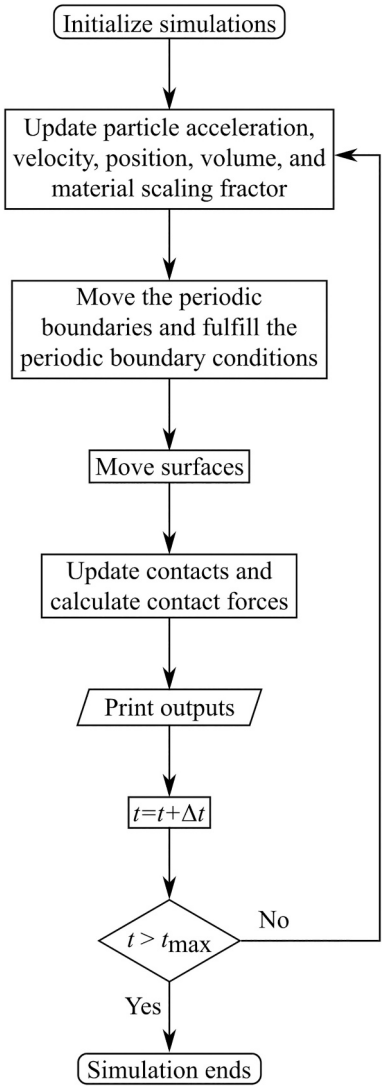


Fig. 2. Flowchart for DEM calculations.

Table 1
Material properties of the active material (NMC) and the CBD (PVDF+CB).

Parameter	Active material [14]	CBD [4]
Young's modulus [GPa]	140	2
Poisson's ratio [−]	0.3	0.3
Yield strength [GPa]	2.9	0.2

The size distribution of the active particles follows the size distribution of a representative NMC powder, measured in our previous study [24]. The cumulative distribution limits of the measured particle size distribution were $x_{10,3} = 8.29$ μm, $x_{16,3} = 9.10$ μm, $x_{50,3} = 12.63$ μm, $x_{84,3} = 16.82$ μm, $x_{90,3} = 17.73$ μm, $x_{99,3} = 23.21$ μm. The particle diameters used in the simulations were limited to the range $d = [9.10, 23.2]$ μm, corresponding values to the size limits $x_{16,3}$ and $x_{99,3}$ respectively of the particle size distribution.

The representative electrode is created in several steps, mimicking the manufacturing process of the electrode, all shown in Fig. 3. Initially, an uncalendered electrode must be created. This is done through a random packing method of the active particles. All the particles are created within the RVE at such a height that allows for a binder contact to be initialised between all particles. The active particles are then

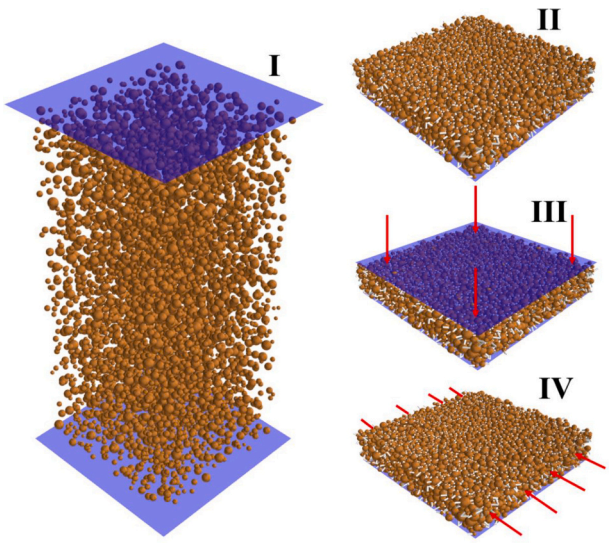


Fig. 3. A schematic figure of the RVE of the positive electrode for the different steps in the simulation process: (I) random packing, (II) uncalendered electrode layer, (III) calendering process, (IV) charge cycling and in-plane mechanical loading. Figure adapted from [23].

packed using gravity until they settle at the bottom of the RVE. During this packing process, the initialisation of the type of contact between two discrete elements is determined. The type of contact to be created is randomly selected, with a 60 % probability of the contact being a CBD contact. The adhesion in the binder contact is not activated during the packing process but is activated when all the particles have settled at the bottom of the RVE. Each simulation was performed four times to capture the stochastic behaviour of the packing process of the RVE and the size distribution of the active particles.

Following the packing process, the electrode is calendered. During the manufacturing of the electrodes, the purpose of the calendering process is to decrease the porosity in the active layer and rearrange its microstructure [33]. This is represented in the framework by compressing the active layer using a rigid surface to a determined calendering height, after which the calendering surface is unloaded and removed. The layer was calendered to a height of 105 μm, which resulted in a maximum calendering pressure of 220 MPa. The calendering process is modelled in a quasistatic fashion, which enables the use of mass scaling, thus decreasing the computational time. This mass scaling approach is also used in all subsequent simulation steps. The calendering process also introduces a residual stress state, which is important for the mechanical behaviour of the electrode. The stress in the RVE is evaluated using a macroscopic stress tensor, which considers all the forces in the contacts as well as the full RVE volume. The complete expression for the stress tensor is presented in [23]. The coordination number for both the particle and CBD contacts, i.e. the total number of particle/CBD contacts normalised by the total number of particles, is also recorded to indicate the packing state of the granular medium. After these two steps, the model represents a manufactured electrode, which can be used for our modelling of the charge cycling process.

A method of determining the in-plane unloading stiffness of the electrode has also been set up. The in-plane stiffness is determined by stretching or compressing the periodic boundary condition in one direction to a prescribed strain level. At the prescribed strain level, a small strain unloading is performed, and the in-plane unloading stiffness is evaluated. The measurements are performed at the strain levels: 0.25 %, 0.5 %, 1 %, 1.5 %, and 2 %, both in compression and tension following, the measurement performed by Gupta and Ucel et al. [5,34].

3.1. Charge cycling

The main objective of this paper was to investigate how charge cycling influenced the mechanical properties of the active layer. Both the volumetric change of the active particles, observed by Parks et al. [9], and the degradation of the active material properties, displayed by Xu et al. [14], were regarded in the simulated charge cycling to see their impact on the mechanical properties of the full electrode layer. The simulated mechanical properties were also compared to the stiffening trend of the layer following cycling, shown in experiments by Gupta et al. [17]. Initially, the change in mechanical properties over the first delithiation of the active layer was investigated.

As reported by Parks et al. [9], the volume of the active particles increased by roughly 20 % over the first delithiation and the material properties (i.e. Young's modulus and hardness/yield strength) decreased by approximately 20 %, following observations by Xu et al. [14]. The first delithiation phase was modelled by linearly increasing the particle radius and decreasing the material scaling factor to the desired levels. The in-plane stiffness is determined after charging to three different SOCs: 0 %, 50 %, and 100 %. The layer at 0 % SOC corresponds to an unaltered electrode layer after the calendering process. The active particle volume ratios, radius ratios and material scaling factors at the various SOCs can be seen in Table 2. Two simulations of the charging process were also performed, with either the material degradation or the particle swelling acting individually to see their impact on the mechanical properties of the full electrode layer.

Following this, the impact of cycling of the electrode layer was investigated. The electrode was subjected to ten charge cycles, and mechanical properties such as the internal stress state, active layer thickness, and the particle coordination number was tracked to see the evolution over cycling. One charge cycle represents charging the battery to 100 % SOC and discharging it to 0 % SOC again. The material properties and the volumetric change of the active particles will be linked to the SOC as well as the cycle number, following the observations of Xu [14] and Parks [9,11].

As stated above, Parks et al. [9] showed that during the first delithiation, the volume of the particles increased by roughly 20 %. This is due to cracks and voids forming in the secondary active particles. In their following study [11], they investigated the damage evolution of the secondary particles over several charge cycles. There, they showed that the damage over the first charge cycle was reversible at the lithiation process but only partially. They did not report the volumetric change explicitly in this study, only the indications of damage. This entails that some residual volume change persists after the first charge cycle, although it is unclear how large. They also determined that the residual damage after the tenth charge cycle increased to a level comparable to that after the first delithiation. Considering this limited experimental insight into the active particle volume evolution over charge cycling, we proposed the following relation for the particle volume over charge cycling.

Over the first delithiation, we prescribe a 20 % volume increase in the active particles. This is also seen as the maximum volume increase for further cycling. We also assume that the volume of the particles after the tenth charge cycle is equal to the volume at the first lithiation, i.e. 120 % of the initial particle volume. At each lithiated stage (at the end of each charge cycle), the residual volume increase of the particles is an interpolated value of the initial and final particle volume. As mentioned above, the volume of the particles is controlled by altering the particle's radius, and between charge states, the particle radius is linearly altered. This results in a non-linear change of the particle volume. This is, however, not considered a concern as the change in radius/volume is not of a considerable degree. As Xu et al. [14] show, the active particles' material depends on both the SOC and the number of cycles. As stated above, the material properties were reduced by roughly 20 % over the first lithiation. After the following lithiation, the material properties increased but not to their initial state. A 10 % residual decrease of the material properties was seen after the first cycle. Over the following charge cycling, the material properties saw a linear decline; however, less severe compared to the reduction over the first charge cycle. After 30 cycles, the material had degraded by roughly 20 %. In our simulation, we use this relation for the material degradation. At the initial delithiation, the material properties are reduced by 20 %. This is seen as the largest material degradation and occurs at the delithiated state of the electrode every charge cycle. The following lithiation increases the material properties by ten percentage points, giving a residual degradation of 10 % after the first charge cycle. After 30 cycles, the material has acquired a residual degradation of 20 %. Between the first cycle and the 30th cycle, the degradation of the material at the lithiated state is interpolated between the state after the first cycle and after the 30th cycle. The particle volume ratio and material scaling for all cycling stages are presented Fig. 4. Three simulations were carried out, during which the electrode was cycled over one, three, and ten cycles before the in-plane stiffness was determined. It should be noted that during these charging simulations, the active layer is unrestricted at the top, allowing it to expand and shrink in the out-of-plane direction.

Table 2
Active particle (NMC) volume ratio [9], radius ratio and active material properties scaling [14] at various SOCs over the first delithiation.

SOC [%]	Volume ratio $\frac{V}{V_0}$	Radius ratio $\frac{R}{R_0}$	Material scaling k
0	1.0	1.0	1.0
50	1.1	1.032	0.90
100	1.2	1.063	0.80

4. Results and discussion

A through investigation of how the mechanical properties of the full positive electrode layer depend on the charge cycling of the cell was performed. Utilising the DEM framework, properties and trends measured in experiments are replicated, and further insight into the mechanical properties of the layer can be provided through properties challenging to measure using experimental techniques, such as the coordination number for the CBD and particle contacts and in-plane compressive stresses. Initially, the first delithiation of the electrode is studied. All the results in the figures are presented with the mean and one standard deviation from the four performed simulations.

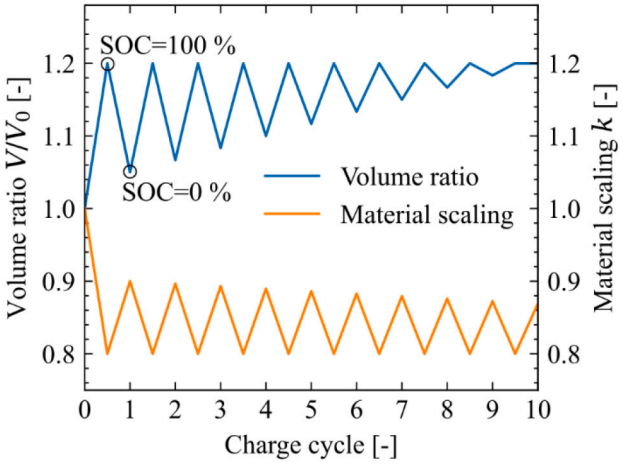


Fig. 4. The particle volume ratio [9,11] and material scaling [14] over all charge cycles.

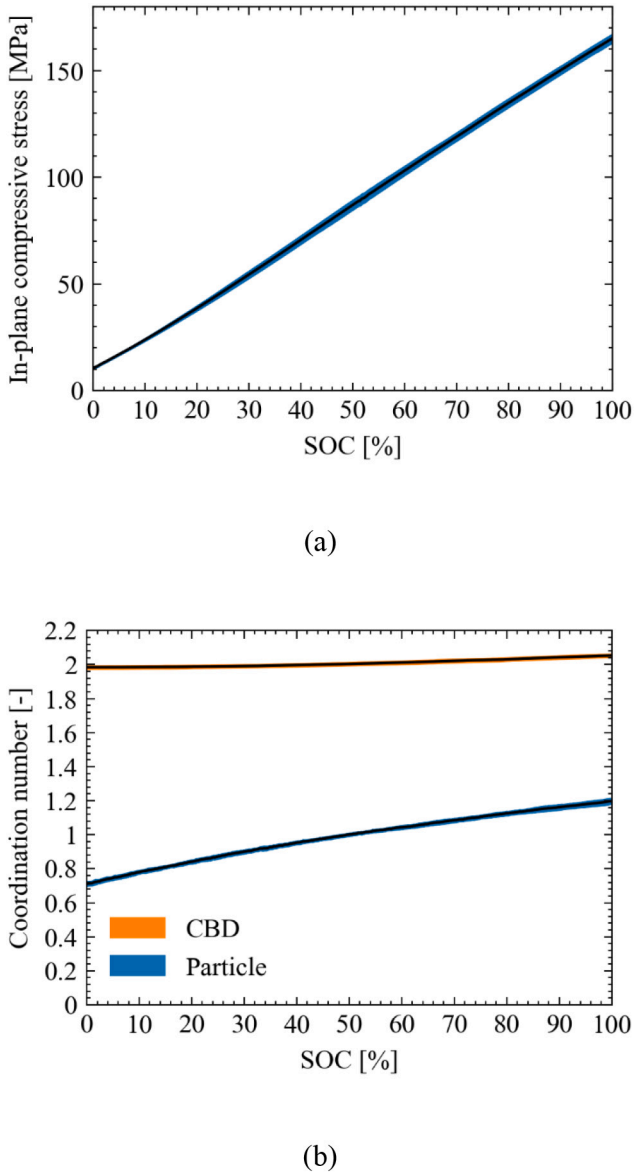


Fig. 5. (a) In-plane compressive stress and (b) coordination number in the electrode layer over the initial charging process.

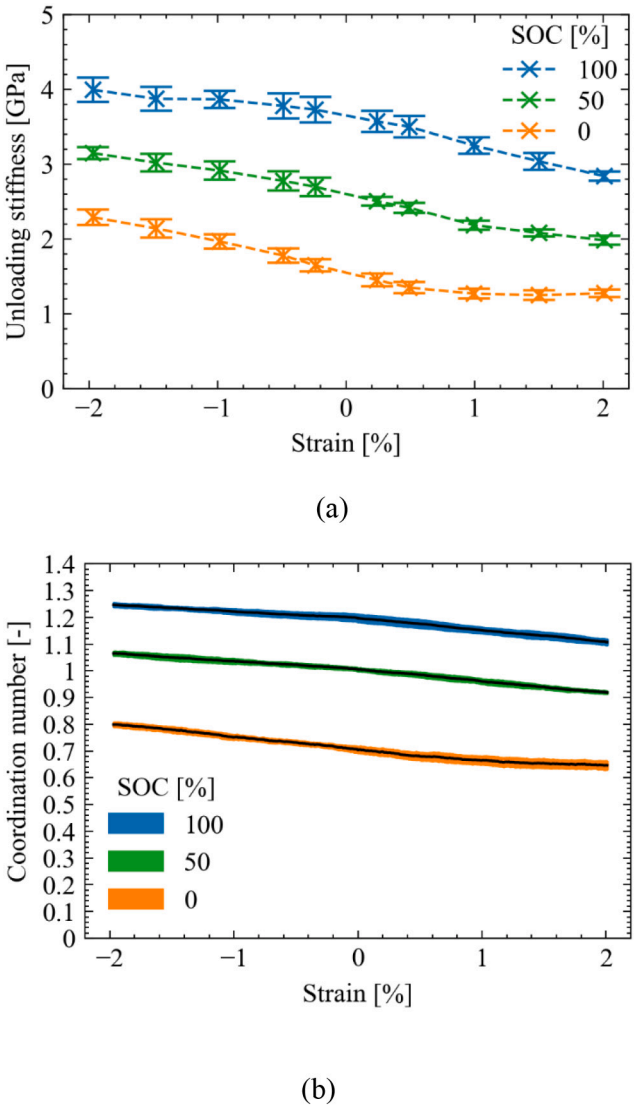
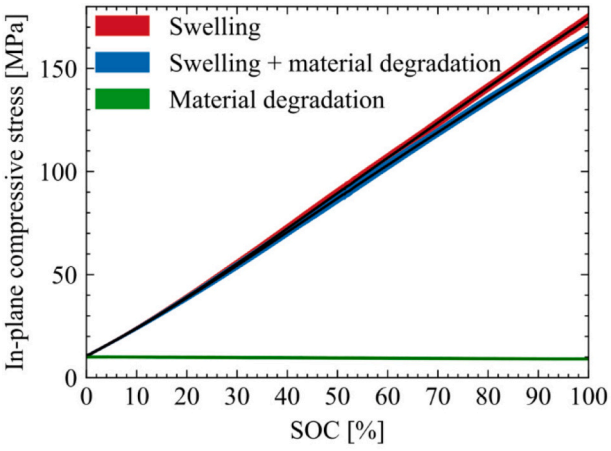


Fig. 6. (a) In-plane stiffness and (b) coordination number for particle contacts of electrode layer at various strain levels at three SOC at the initial delithiation.

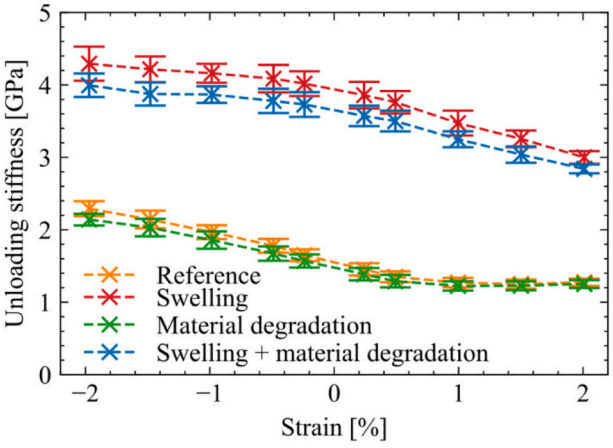
4.1. First delithiation

After an electrode layer had been created and calendered, as described in the previous chapter and our previous studies [23,24], the initial charging process was investigated. Over the charging process, the in-plane compressive stress increased in a linear manner, see Fig. 5 (a). An average initial compressive stress of 10 MPa in the layer can also be observed at 0 % SOC, i.e. after the calendering process. The increase of the in-plane compressive stress results from the expansion of the active particles. This also leads to an increased particle coordination number, which can be seen in Fig. 5 (b). The expansion of the active particles over charging also increases the in-plane stiffness, see Fig. 6 (a). The behaviour of a constant stiffness at all tension levels and an increasing stiffness at increasing compression levels, a trend observed in our previous studies [23,24] and through experimental measurements [5], can be seen at 0 % SOC. However, this trend disappeared at 50 % and 100 % SOC. This as the initial particle coordination number before the mechanical loading increases with the expanding particles, as seen in Fig. 6 (b), similar to when the electrode is compressed. When the layer then is loaded in tension, the particle coordination number decreases which results in a decrease in the layer stiffness. This differs from the uncharged layer (0 % SOC), where the particle coordination number at all tension levels is relatively constant.

As the delithiation process incorporates both the volume expansion of the active particles and the degradation of the active particle material, the impact of each phenomenon on the mechanical properties was investigated. The charging simulations were performed either with the swelling of the active particles or the degradation of the active particle material. Fig. 7 (a) shows the in-plane stress of the charging simulations with active particle volumetric expansion, active material degradation, and the two phenomena combined. The increase in in-plane compressive stress for the simulations with active particle swelling and active particle swelling and material degradation was comparable. The increase of in-plane compressive stress was lower with both phenomena active due to the diminished mechanical properties of the active material. As for the layer with only active material degradation, the in-plane compressive stress decreased slightly. However, the stress was relatively constant in relation to the stress increase stemming from the particle swelling. This trend also translated to the determined in-plane stiffness of the layers, seen in Fig. 7 (b). The layer with swelling active particles and material degradation and the layer with only swelling active particles give a comparable stiffness level and trend in compression and



(a)



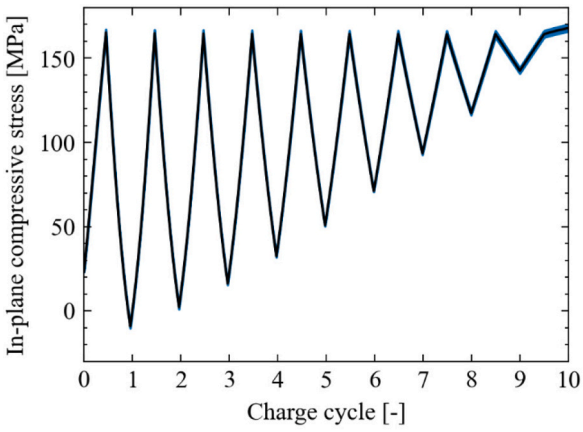
(b)

Fig. 7. (a) In-plane compressive stress over the initial charging process and (b) in-plane stiffness of the electrode layer at 100 % SOC with active particle swelling and material degradation separated and combined.

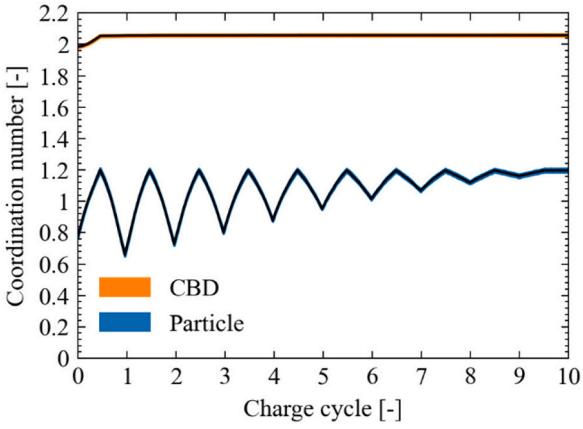
tension. The layer with active material degradation showed comparable results to the reference layer (i.e. a layer at 0 % SOC), except for a slight decrease in the in-plane stiffness stemming from the degraded active material. However, the stress was essentially constant in comparison to the stress increase stemming from the particle swelling. This demonstrates that the volume expansion of the particles has a significantly greater impact on the in-plane compressive stress and stiffness of the electrode layer compared to the material degradation.

4.2. Charge cycling

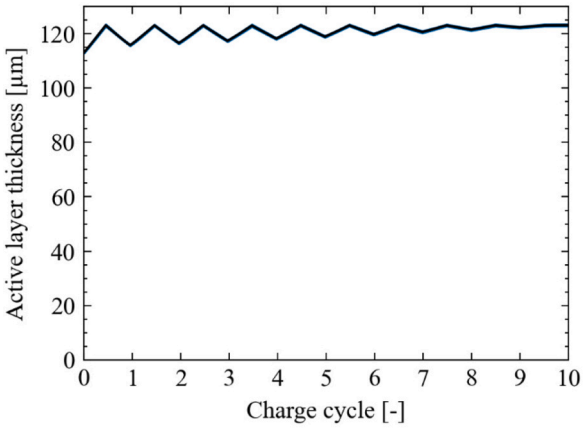
The evolution of the mechanical properties over charge cycling was now investigated. The in-plane compressive stress over the ten charge cycles can be seen in Fig. 8 (a), which shows a clear correlation between the SOC, and thus the volumetric expansion and material degradation of the active particles, and the in-plane compressive stress. The layer thickness over charge cycling is shown in Fig. 8 (c), where it is also evident that the thickness of the layer is correlated to the volumetric expansion of the active particles, where the active layer increased in thickness with increased active particle volume expansion. A similar



(a)



(b)



(c)

Fig. 8. (a) In-plane compressive stress, (b) coordination number, and (c) active layer thickness over charge cycling.

trend of increased thickness of the active layer over charge cycling was observed by Gupta et al. [17] The cyclic charging also shows an interesting interplay between the expanding/shrinking active particles and the elastic-plastic CBD. After the first discharge, i.e. after one charge cycle, the residual in-plane stress state has transitioned from a compressive to a tensile state, see Fig. 8 (a). This is due to the expanding active particles compressing the CBD, introducing plastic deformations, new CBD contacts forming, and plastic deformation occurring in particles in contact with other particles. When the active particles after that reduce in size during the discharging phase, the CBD is loaded in tension and particles in contact detach. This can be seen in Fig. 8 (b), where the number of CBD contacts increases over the first charging phase, and the number of particle contacts decreases after the first charge cycle compared to its initial number. After continued cycling, the residual in-plane stress state transfers to a compressive state due to the irreversible swelling of the active particles after the discharge process, and the residual in-plane compressive stress increases for each charge cycle. This irreversible swelling also shows an increase in the particle coordination number after each charge cycle, see Fig. 8 (b). This also manifests in the determined in-plane stiffness after increasing the number of charge cycles, see Fig. 9 (a).

After one charge cycle, the stiffness had increased at all strain levels compared to the uncycled layer. The trend of constant stiffness at various tension levels is also more prominent compared to the uncycled layer. This is due to the increase in CBD coordination number while the particle coordination number has decreased, which results in the mechanical properties of the layer being governed by the CBD to a greater extent. After three charge cycles, both the particle and CBD coordination numbers have increased compared to their initial values. This leads to increased stiffness at all strain levels. After ten charge cycles, the particle coordination number has increased drastically compared to the uncycled layer, and the increase of particle contacts has stagnated due to the lower amplitude of the irreversible volumetric change of the active particles. This severe increase in the number of particles in contact also increases the layer stiffness. The trend of increased stiffness with increased number of charge cycles matches with experimental measurements performed on comparable electrode layers by Gupta et al. [17], and the results presented in this study indicate that the stiffness increase is caused by the volumetric expansion of the active particles. A comparison of the electrode layer after ten charge cycles and the layer after the first charge at 100 % SOC indicates that the two layers have similar mechanical states. Both in terms of CBD and particle coordination numbers and the in-plane stress state, and mechanical properties in terms of the in-plane stiffness. This as the volumetric expansion and material degradation at these stages are similar, thus showing that the mechanical properties are not influenced by the cyclic loading to a large extent but instead more dependent on the swelling state of the active particles and their degree of material degradation.

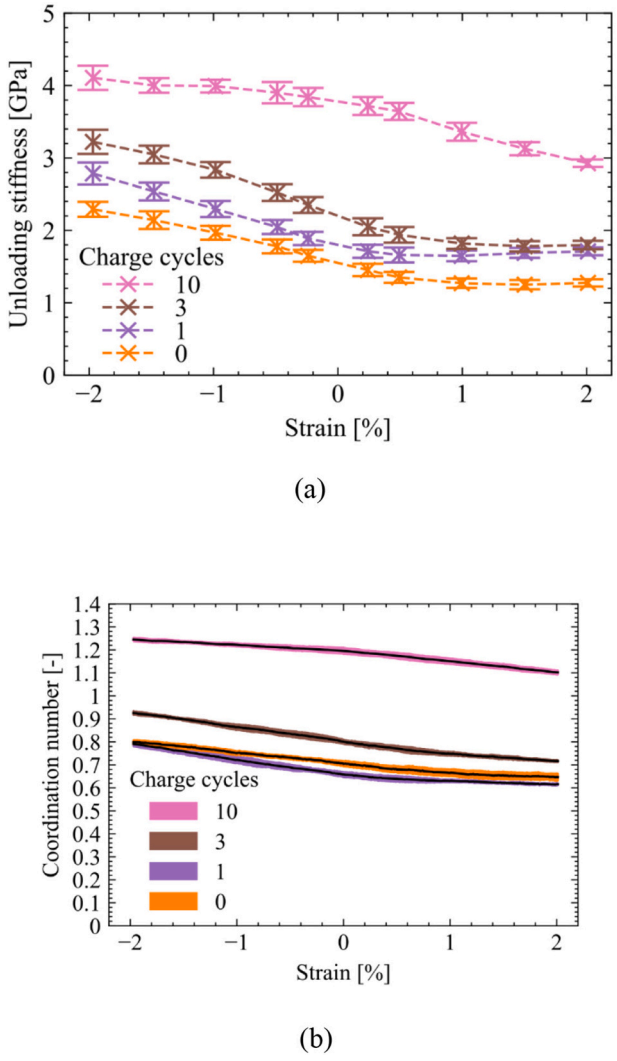


Fig. 9. (a) In-plane stiffness and (b) particle coordination number of the electrode layer at varous strain levels after charge cycles.

If this conclusion is accurate in real electrode layers is difficult to determine based on the current experimental results presented in the literature. It is evident that the in-plane stress state depends on the active particles' volumetric change and their mechanical properties. However, it is likely that the modelling of the expansion and degradation of the active particles performed in this study does not fully capture the true behaviour of the electrode constituents. One example is the assumption of quasistatic homogeneous volumetric change of the active particles over the charge cycling. This assumption relies on the notion that fracture within the secondary NMC particle is not linked to the de−/intercalation rate and that the lithiation distribution in the out-of-plane direction is homogeneous. This is, however, not the case, as the fracture of the particles is linked to both its position in the layer and the C-rate of the charge cycling. Particles at the top of the active layer are more prone to fracture due to exposure to higher lithium-ion concentrations, as lithium-ion diffusion through the layer is limited by the high tortuosity of the CBD, something shown by Parks et al. [9]. High C-rates also result in increased cracking, as higher gradients of volumetric change arise within the secondary particles. This could also result in a stress gradient in the out-of-plane direction of the layer, where the greater volumetric expansion of the active particles at the top of the layer would induce a greater in-plane compressive stress as well. The modelling framework could be extended to capture this behaviour if accurate measurements of the particle expansion dependent on the C-rate and position in the layer were available in the literature. Furthermore, the in-plane pressure increases over the last discharge of the charge cycling, which is seen in Fig. 8 (a). This pressure increase occurs as the volume of the particles is set to be constant, but active material sees a recovery in its material properties. The increase in active material stiffness and yield strength increases the in-plane pressure of the layer. There is a possibility that the full extent of loss of the contact properties is not captured through the indentation experiments of the active material at an increasing number of charge cycles, as the indentation only measures on the material scale and does not capture macroscopic defects such as cracks and voids in the secondary particles. An experimental investigation of the compression of the active particles after charge cycling would be beneficial in validating the modelling assumptions, something which has not been explored in the literature to the author's knowledge. The modelling of degradation of the mechanical properties of the CBD could also be improved by including fracture. This would allow capturing phenomena such as delamination and island formation within the electrode, which are well-known damage phenomena. These aspects of damage and

fracture of the electrode layer stemming from the fracture of the active particles and the CBD will be the focus of upcoming studies.

5. Conclusions

This study utilised and expanded a DEM modelling framework developed to investigate the mechanical properties of a positive electrode active layer. The evolution of mechanical properties of the layer due to charge cycling was the main focus of this study with the most important conclusions being:

- The volumetric change and degradation of the material of the active particles over charge cycling altered the mechanical properties of the full electrode layer.
- The volumetric change of the active particles governs the mechanical properties of the active layer to a greater extent than the active material degradation.
- Over charge cycling, the stiffness of the active layer increased following the irreversible expansion of the active particles.
- All the issues above are captured well by the DEM modelling framework and enable possibilities for the optimisation of the mechanical properties of the electrode layer with respect to the electrode constituents and its manufacturing process.

CRediT authorship contribution statement

Axel Lundkvist: Writing – review & editing, Writing – original draft, Visualization, Software, Methodology, Formal analysis, Conceptualization. **Per-Lennart Larsson:** Writing – review & editing, Writing – original draft, Supervision, Conceptualization. **Erik Olsson:** Writing – review & editing, Writing – original draft, Supervision, Software, Funding acquisition, Conceptualization.

Declaration of competing interest

The authors declare that they have no known competing financial interests or personal relationships that could have appeared to influence the work reported in this paper.

Acknowledgements

The authors would like to acknowledge Prof. Peter Gudmundson and Prof. Artem Kulachenko for helpful discussions, and Energimyndigheten (the Swedish Energy Agency) for financing the project through the grant 46558-1.

Data availability

The code is shared on GitHub: https://github.com/axlun/DEMsim.

References

[1] J.S. Edge, et al., Lithium ion battery degradation: what you need to know, Phys. Chem. Chem. Phys. 23 (14) (2021) 8200–8221, https://doi.org/10.1039/d1cp00359c.
[2] A. Mukhopadhyay, B.W. Sheldon, Deformation and stress in electrode materials for li-ion batteries, Prog. Mater. Sci. 63 (January) (2014) 58–116, https://doi.org/10.1016/j.pmatsci.2014.02.001.
[3] V. Nagda, H. Ekström, A. Kulachenko, Impact of mechanical degradation in polycrystalline NMC particle on the electrochemical performance of Lithium-ion batteries, J. Electrochem. Soc. 171 (2024), https://doi.org/10.1149/1945-7111/ad5622.
[4] A.H.S. Iyer, P. Gupta, P. Gudmundson, A. Kulachenko, Measuring microscale mechanical properties of PVdF binder phase and the binder-particle interface using micromechanical testing, Mater. Sci. Eng. A 881 (May) (2023) 145352, https://doi.org/10.1016/j.msea.2023.145352.
[5] P. Gupta, I.B. Üçel, P. Gudmundson, E. Olsson, Characterization of the constitutive behavior of a cathode active layer in Lithium-ion batteries using a bending test method, Exp. Mech. 60 (6) (2020) 847–860, https://doi.org/10.1007/s11340-020-00613-5.
[6] P. Gupta, P. Gudmundson, Modeling of local electrode stresses and pressures in lithium-ion battery packs using three-dimensional homogenization, J. Power Sources 582 (July) (2023) 233514, https://doi.org/10.1016/j.jpowsour.2023.233514.
[7] D. Dang, Y. Wang, Y.-T. Cheng, Communication—fracture behavior of single LiNi 0.33 Mn 0.33 co 0.33 O 2 particles studied by flat punch indentation, J. Electrochem. Soc. 166 (13) (2019) A2749–A2751, https://doi.org/10.1149/2.0331913jes.
[8] L. De Biasi, A.O. Kondrakov, H. Geßwein, T. Brezesinski, P. Hartmann, J. Janek, Between Scylla and Charybdis: balancing among structural stability and energy density of layered NCM cathode materials for advanced Lithium-ion batteries, J. Phys. Chem. C 121 (47) (2017) 26163–26171, https://doi.org/10.1021/acs.jpcc.7b06363.
[9] H.C.W. Parks, et al., Direct observations of electrochemically induced intergranular cracking in polycrystalline NMC811 particles, J Mater Chem A 11 (39) (2023) 21322–21332, https://doi.org/10.1039/d3ta03057a.
[10] P.C. Tsai, et al., Single-particle measurements of electrochemical kinetics in NMC and NCA cathodes for li-ion batteries, Energy Environ. Sci. 11 (4) (2018) 860–871, https://doi.org/10.1039/c8ee00001h.
[11] H.C.W. Parks, et al., Non-linear cracking response to voltage revealed by operando X-ray tomography in polycrystalline NMC811, EES Batter. (2025), https://doi.org/10.1039/D5EB00008D.
[12] A. Wade, et al., First cycle cracking behaviour within Ni-rich cathodes during high-voltage charging, J. Electrochem. Soc. 170 (7) (2023) 070513, https://doi.org/10.1149/1945-7111/ace130.
[13] S.S. Shishvan, N.A. Fleck, R.M. McMeeking, V.S. Deshpande, Cracking and associated volumetric expansion of NMC811 secondary particles, J. Power Sources 588 (August) (2023) 233745, https://doi.org/10.1016/j.jpowsour.2023.233745.
[14] R. Xu, H. Sun, L.S. de Vasconcelos, K. Zhao, Mechanical and structural degradation of LiNi x Mn y co z O 2 cathode in li-ion batteries: an experimental study, J. Electrochem. Soc. 164 (13) (2017), https://doi.org/10.1149/2.1751713jes pp. A3333–A 3341.
[15] F.B. Spingler, S. Kücher, R. Phillips, E. Moyassari, A. Jossen, Electrochemically stable in situ dilatometry of NMC, NCA and graphite electrodes for Lithium-ion cells compared to XRD measurements, J. Electrochem. Soc. 168 (4) (2021) 040515, https://doi.org/10.1149/1945-7111/abf262.
[16] D. Sauerteig, S. Ivanov, H. Reinshagen, A. Bund, Reversible and irreversible dilation of lithium-ion battery electrodes investigated by in-situ dilatometry, J. Power Sources 342 (2017) 939–946, https://doi.org/10.1016/j.jpowsour.2016.12.121.
[17] P. Gupta, M. Streb, A. Siddiqui, M. Klett, G. Lindbergh, P. Gudmundson, Layer-resolved mechanical degradation of a Ni-rich positive electrode, Batteries 9 (12) (2023) 1–18, https://doi.org/10.3390/batteries9120575.
[18] J. Xu, et al., Lithium ion battery electrode manufacturing model accounting for 3D realistic shapes of active material particles, J. Power Sources 554 (October) (2022) 2023, https://doi.org/10.1016/j.jpowsour.2022.232294.
[19] C. Sangrós Giménez, L. Helmers, C. Schilde, A. Diener, A. Kwade, Modeling the electrical conductive paths within all-solid-state battery electrodes, Chem. Eng. Technol. 43 (5) (2020) 819–829, https://doi.org/10.1002/ceat.201900501.
[20] A.C. Ngandjong, et al., Investigating electrode calendering and its impact on electrochemical performance by means of a new discrete element method model: towards a digital twin of li-ion battery manufacturing, J. Power Sources 485 (2021) 229320, https://doi.org/10.1016/j.jpowsour.2020.229320.
[21] D. Schreiner, J. Lindenblatt, R. Daub, G. Reinhart, Simulation of the Calendering process of NMC-622 cathodes for Lithium-ion batteries, Energ. Technol. (2022), https://doi.org/10.1002/ente.202200442.
[22] C. Sangrós Giménez, C. Schilde, L. Froböse, S. Ivanov, A. Kwade, Mechanical, electrical, and ionic behavior of Lithium-ion battery electrodes via discrete element method simulations, Energ. Technol. 8 (2) (2020) 1–10, https://doi.org/10.1002/ente.201900180.
[23] A. Lundkvist, P.L. Larsson, E. Olsson, A discrete element analysis of the mechanical behaviour of a lithium-ion battery electrode active layer, Powder Technol. 425 (March) (2023) 118574, https://doi.org/10.1016/j.powtec.2023.118574.
[24] A. Lundkvist, P.L. Larsson, A.H.S. Iyer, E. Olsson, Discrete element modelling of the elastic-plastic and viscoelastic properties of a lithium-ion battery electrode layer, Powder Technol. 443 (May) (2024) 119873, https://doi.org/10.1016/j.powtec.2024.119873.
[25] K.L. Johnson, The correlation of indentation experiments, J. Mech. Phys. Solids 18 (2) (1970) 115–126, https://doi.org/10.1016/0022-5096(70)90029-3.
[26] H. Hertz, Ueber die Berührung fester elastischer Körper, J. Reine Angew. Math. 1882 (92) (1882) 156–171, https://doi.org/10.1515/crll.1882.92.156.
[27] S. Biwa, B. Storåkers, An analysis of fully plastic Brinell indentation, J. Mech. Phys. Solids 43 (8) (1995) 1303–1333, https://doi.org/10.1016/0022-5096(95)00031-D.
[28] B. Storåkers, S. Biwa, P.L. Larsson, Similarity analysis of inelastic contact, Int. J. Solids Struct. 34 (24) (1997) 3061–3083, https://doi.org/10.1016/S0020-7683(96)00176-X.

[29] B. Storåkers, Local contact behaviour of Viscoplastic particles, in: IUTAM Symposium on Mechanics of Granular and Porous Materials vol. 1997, 1996, pp. 173–184, https://doi.org/10.1007/978-94-011-5520-5_16.
[30] E. Olsson, P.L. Larsson, On the appropriate use of representative stress quantities at correlation of spherical contact problems, Tribol. Lett. 50 (2) (2013) 221–232, https://doi.org/10.1007/s11249-013-0114-1.
[31] E. Olsson, P.L. Larsson, A unified model for the contact behaviour between equal and dissimilar elastic-plastic spherical bodies, Int. J. Solids Struct. 81 (2016) 23–32, https://doi.org/10.1016/j.ijsolstr.2015.10.004.
[32] E. Olsson, P.L. Larsson, On the effect of particle size distribution in cold powder compaction, J. Appl. Mech. Trans. ASME 79 (5) (2012), https://doi.org/10.1115/1.4006382.
[33] A. Kwade, W. Haselrieder, R. Leithoff, A. Modlinger, F. Dietrich, K. Droeder, Current status and challenges for automotive battery production technologies, Nat. Energy 3 (4) (2018) 290–300, https://doi.org/10.1038/s41560-018-0130-3.
[34] B. Üçel, P. Gupta, P. Gudmundson, Experimental determination of the constitutive properties of a graphite anode layer in lithium-ion batteries using a bending test method, J Energy Storage 46 (February 2021) (2022) 103845, https://doi.org/10.1016/j.est.2021.103845.